



CHORUS

This is the accepted manuscript made available via CHORUS. The article has been published as:

Pressure-induced anomalous enhancement of insulating state and isosymmetric structural transition in quasi-one-dimensional TiS_3

Chao An, Pengchao Lu, Xuliang Chen, Yonghui Zhou, Juefei Wu, Ying Zhou, Changyong Park, Chuanchuan Gu, Bowen Zhang, Yifang Yuan, Jian Sun, and Zhaorong Yang

Phys. Rev. B **96**, 134110 — Published 16 October 2017

DOI: [10.1103/PhysRevB.96.134110](https://doi.org/10.1103/PhysRevB.96.134110)

**Pressure-induced anomalous enhancement of insulating state
and novel iso-symmetric structural transition in
quasi-one-dimensional TiS₃**

Chao An^{1,2}, Pengchao Lu³, Xuliang Chen¹, Yonghui Zhou¹, Juefei Wu³, Ying Zhou^{1,2},
Changyong Park⁴, Chuanchuan Gu¹, Bowen Zhang^{1,2}, Yifang Yuan^{1,5}, Jian Sun^{3,6,†},
Zhaorong Yang^{1,6,†}

¹*Anhui Province Key Laboratory of Condensed Matter Physics at Extreme Conditions, High
Magnetic Field Laboratory, Chinese Academy of Sciences, Hefei 230031, China*

²*University of Science and Technology of China, Hefei 230026, China*

³*National Laboratory of Solid State Microstructures, School of Physics, Nanjing University,
Nanjing 210093, China*

⁴*HPCAT, Geophysical Laboratory, Carnegie Institution of Washington, Argonne 60439, USA*

⁵*Department of Physics and Engineering, Zhengzhou University, Zhengzhou 450052, China*

⁶*Collaborative Innovation Center of Advanced Microstructures, Nanjing 210093, China*

[†]E-mails: zryang@issp.ac.cn; jiansun@nju.edu.cn

Abstract

We present *in situ* high-pressure synchrotron X-ray diffraction (XRD) and electrical transport measurements on quasi-one-dimensional single crystal TiS_3 up to 29.9-39.0 GPa in diamond anvil cells, coupled with first-principles calculations. Counter-intuitively, the conductive behavior of semiconductor TiS_3 becomes increasingly insulating with pressure till $P_{C1} \sim 12$ GPa, where extremes in all the three axial ratios are observed. Upon further compression to $P_{C2} \sim 22$ GPa, the XRD data evidences a structural phase transition. Based on our theoretical calculations, this structural transition is determined to be iso-symmetric, i.e. without change of the structural symmetry ($P2_1/m$), mainly resulted from rearrangement of the dangling S_2 pair along the a axis.

I. INTRODUCTION

Titanium tri-sulfide (TiS_3), with a direct and sizeable band gap (~ 1.0 eV) and predicted ultrahigh mobility (10^4 $\text{cm}^2/\text{V s}$) [1,2], has attracted much attention recently for a wide variety of applications. It is made of TiS_3 layers held together by weak van der Waals forces, where each layer is composed of weakly interacting quasi-one-dimensional (Q1D) chains of TiS_3 triangular prisms extending along b axis. The weak connecting nature of the lattice makes TiS_3 flexible in fabricating nanosheets-like transistors with tailored morphology and electrical properties [3] or nanoribbon-based transistors with a record high breakdown current density of 1.7×10^6 A cm^{-2} [4]. In the case of monolayer, TiS_3 is predicted to exhibit good light absorption in the visible-light region [5], indicating its great potential in optical devices. In addition, TiS_3 has also potential applications in other fields, such as solar cells and thermoelectric conversion devices [6,7], photoelectrochemical cells [8], as well as cathodes in batteries [9].

Originated from its Q1D structural character, layered TiS_3 exhibits strong in-plane anisotropy in optical absorption [10], mobility [3] and thermoelectric properties [6]. Such unique lattice structure also holds promise for tailoring the band gap and exploring novel properties by strain engineering. First-principles calculations reveal that the gap of TiS_3 is almost independent on layer thickness, vertical (c axis) compressive strain and stacking order [11], in contrast to the case of some other layered materials such as MoS_2 [12]. For monolayer and bilayer TiS_3 , calculations show that the gap increases (decreases) when a uniaxial tensile (compressive) strain is applied along the b axis [13-15]. In addition, upon further compression along the b axis, a direct to indirect gap transition is predicted. Very recently, the vibrational properties of Q1D TiS_3 were investigated through high-pressure Raman spectroscopy as well as theoretical calculations [16]. Remarkably, only out-of-plane vibrational Raman-active modes are observed and some of them involve unique rigid-chain vibrations and S-S molecular oscillations. Moreover, a negative pressure dependence

of the highest frequency mode is revealed. To date, since experimental studies on the high-pressure electronic properties are still lacking, how these unconventional vibrations reflect on the structural and electronic properties remains unclear.

In this paper, the above mentioned issues are addressed with *in situ* high-pressure synchrotron X-ray diffraction (XRD) and electrical transport measurements on single crystal TiS_3 , combined with first-principles calculations. The resistance measurement shows that an anomalous increasingly insulating state is observed under pressure up to $P_{CI} \sim 12$ GPa. Meanwhile, we find that all the axial ratios display extremes at P_{CI} . According to the first-principles calculations, the separation of the dangling S_2 pair along the a axis becomes larger and larger with pressure, which may give rise to these anomalies observed at P_{CI} . Furthermore, a novel iso-symmetric structural transition around $P_{C2} \sim 22$ GPa is revealed from our XRD and theoretical calculations, mainly attributed to pressure-driven re-arrangement of the dangling S_2 pair.

II. EXPERIMENTAL AND CALCULATION METHODS

TiS_3 single crystals were grown by chemical vapor method using I_2 as transport agent [17-18], and the high quality of the crystals were checked by in-house single crystal XRD ($\text{Cu } K_\alpha$, $\lambda = 1.54184 \text{ \AA}$) and EDX (see APPENDIX A for more details). Standard four-probe method was employed to perform the high-pressure electrical transport measurements in a temperature range of 5-300 K in a Be-Cu diamond anvil cell using h-BN as transmitting medium. A sample ($\sim 80\mu\text{m} \times 30\mu\text{m} \times 5\mu\text{m}$) cleaved from bulk TiS_3 was loaded and the current was introduced along the b axis of the sample inside the cell. High pressure synchrotron powder XRD ($\lambda = 0.4246 \text{ \AA}$) was performed at room temperature at 16 BM-D [19], HPCAT. Daphne 7373 was used as transmitting medium. The DIOPTAS [20] program was used for image integrations and Le Bail method was employed to fit the XRD data with the RIETICA [21] program. Ruby fluorescence method [22] was used to determine the pressure for all of the above experiments.

The structural optimization and phonon calculations are performed by the Vienna Ab initio simulation package (VASP) [23] code, with the generalized gradient approximation Perdew-Burke-Ernzerhof (GGA-PBE) [24] exchange-correlation functionals. A kinetic energy cutoff of the plane wave basis of 400 eV and a $12 \times 16 \times 8$ Monkhorst-Pack k-point mesh are used. The van der Waals (vdW) interaction is carefully taken into account by Grimme's DFT-D2 method [25]. The atomic positions are relaxed until the Hellmann-Feynman forces are within $0.001 \text{ eV}/\text{\AA}$. Transition barriers are calculated through the variable-cell nudged elastic band (VC-NEB) method [26] implemented in the USPEX code [27]. The phonon calculations are performed by supercell approach implemented in the PHONOPY code [28] with a $3 \times 3 \times 2$ supercell and a $3 \times 4 \times 3$ k-point mesh for Brillouin zone integration for the low- and high-pressure structures.

III. RESULTS AND DISCUSSION

Figure 1 displays the temperature (T) dependence of the electrical resistance of the TiS_3 single crystal along the b axis under various pressures. TiS_3 is known as a direct bandgap semiconductor at ambient pressure [1, 29]. With the application of pressure, the original semiconducting behavior ($dR/dT < 0$) of single crystal TiS_3 first becomes more and more insulating [Fig. 1(a)]. The resistance globally gets enhanced and reaches a maximum at 12.5 GPa. Upon further compression, the resistance then begins to decrease gradually but remains a semiconducting-like ($dR/dT < 0$) behavior over the entire temperature range, as displayed in Fig. 1(b). At 25.4 GPa, as shown in the inset of Fig. 1(c), upon warming a partial upturn of resistance ($dR/dT > 0$) is observed above 130 K, indicating occurrence of metallization. The metallic behavior becomes dominant as the pressure continues to increase to the highest pressure of 39.0 GPa.

To understand the unusual pressure enhanced insulating behavior, we performed *in situ* high-pressure synchrotron XRD measurements on TiS_3 ($\lambda = 0.4246 \text{ \AA}$). The

experimental patterns are presented in Fig. 2(a). It is found that the ambient monoclinic phase of TiS_3 (space group $P2_1/m$, labeled as Phase I) is stable under pressure up to 15.4 GPa. When the pressure goes up to 22.4 GPa, however, several new peaks show up as indicated by arrows, suggesting the appearance of a structural transition. We note that in a previous high-pressure Raman study of TiS_3 [16], the doubly degenerate Raman mode A_g^{s-s} splits quite evidently at 24.2 GPa due to lifting of its degeneracy, which should be related to the structural transition. Upon decompression back to 0.2 GPa (denoted by D, top of Fig. 2(a)), the XRD profile evolves back to the starting structure, implying that this structural transition is reversible. Here, it is worthy of mentioning that the XRD peaks begin to broaden gradually above ~ 3.4 GPa [Fig. 2(a)]; in addition, while the above-observed metallization of TiS_3 is accompanied by the structural transition, an upturn behavior at low temperatures in the resistance versus temperature curve [Fig. 1 (c)] still remains in a very broad pressure range of 25.4-39.0 GPa. These experimental observations could be related to the presence of deviatoric stresses the sample inside the DAC experience [30], since Daphne 7373 and h-BN are used as the pressure transmitting media in the synchrotron XRD and electrical transport experiments, respectively.

From the following first-principles calculations, the high pressure structure of TiS_3 is identified as a new phase (labeled as Phase II), which has the same space group ($P2_1/m$) as Phase I. Accordingly, we carried out standard Rietveld refinement using the Le Bail method. Selected refinement results at 0.5 and 25.8 GPa are displayed in Fig. 2(a) (red lines). The detailed lattice parameters as a function of pressure are exhibited in Fig. 2(b). In Phase I, all of the lattice parameters a , b and c , decrease gradually with pressure. The parameter c decreases apparently faster than the others, as the vdW interaction is the weakest along this direction. The volume versus pressure data (EoS) for Phase I and II are plotted in Fig. 1(c). The EoS was fitted by using the third-order Birch-Murnaghan formula [31]:

$$P = \frac{3}{2}B_0[(V_0/V)^{\frac{7}{3}} - (V_0/V)^{\frac{5}{3}}]\{1 + \frac{3}{4}(B_0' - 4)[(V_0/V)^{\frac{2}{3}} - 1]\} \quad (1)$$

where V_0 , B_0 and B'_0 are the volume, bulk modulus $-V/(dV/dP)$, and first order derivative of the bulk modulus at zero pressure, respectively. The fitting yields $V_0 = 147.5 \text{ \AA}^3$, $B_0 = 68.6 \text{ GPa}$, and $B'_0 = 3.4$ for Phase I; and 136 \AA^3 , 74.4 GPa and 4.2 for Phase II. In addition, the volume collapse is estimated to be about 5% over the transition, indicating a first order structural transition.

The structural optimization calculations reveal that the ambient $P2_1/m$ structure (Phase I) transfers into a new one (Phase II) which belongs to the same space group during compression. Nevertheless, there are still some differences between these two phases, mainly in the arrangement of S-S bonds, as illustrated in Fig. 3(a). Such differences can be classified into an unusual iso-symmetric structural transition for TiS_3 under pressure. In Phase I, there are two types of S atoms: one is called as bridge S atoms that is bonded to two neighboring Ti atoms, and the other is referred to as dangling S_2 pair that are bonded to a same Ti atom. In Phase II, the bonding of bridge S to Ti atoms stays unchanged. Since the distance of the S_2 pair ($> a/2$) in Phase II is much larger than that in Phase I ($< a/2$), when the transition occurs, the S-S bond between the dangling S_2 pair is broken and a new bond forms between S atoms that connect with two different Ti atoms, thus a “ Ti_2S_3 ring” is composed from the view along the b axis [lower panel of Fig. 3(a)]. The calculated atomic positions of TiS_3 at zero and 30 GPa are listed in Table I.

Figure 3(b) displays the calculated enthalpy of these two phases under pressure. The theoretical critical pressure is around 16 GPa, above which the Phase II becomes thermodynamically stable. Since the structural transition involves only subtle changes in atoms configurations, the transition barrier should be small. As shown in the inset of Fig. 3(b), our nudged elastic band (NEB) calculations give the estimated barriers to be 16 meV/atom at 15 GPa and 5 meV/atom at 20 GPa. The critical pressure in experiments is slightly higher than our predicted one, which may be on account of the transition barrier. On the other hand, phonon dispersion calculations reveal that Phase

II is dynamically stable at 0 GPa and 20 GPa [see Fig. S2]. However, small transition barrier and large enthalpy difference at low pressure [Fig. 3(b)] suggests that the transition between Phase I and II is reversible when the pressure is released, in accordance with our experimental data as displayed in Fig. 2(a).

Once we combine the above electrical transport and XRD data, it clearly reveals a close relationship between the resistance and lattice axial ratio under pressure, as outlined in Fig. 4. With increasing pressure, the most insulating state is observed around P_{C1} and the metallic feature emerges above P_{C2} . Consistently, the lattice parameters ratios c/a , c/b or a/b exhibit a minimum or maximum at P_{C1} , followed by discontinuities at P_{C2} due to the structural transition. Actually, extremes of lattice axial ratios in the absence of structural transition were also observed in pressurized topological insulators such as Bi_2Te_3 [32], Sb_2Te_3 [33] and Ag_2Te [34], which is taken as signatures of a pressure-induced electronic topological transition.

Intuitively, applying pressure to a semiconductor can generally enhance the overlap of electronic orbitals and decrease the bandgap, leading to metallization or even inducing superconductivity. The enhancement of the insulating state under high pressure is quite unusual. Nevertheless, similar pressure-enhanced insulating state was also reported in $\text{Eu}_2\text{Sn}_2\text{O}_7$ [35] and $\text{Ba}_{1-x}\text{R}_x\text{IrO}_3$ ($R=\text{Gd}, \text{Eu}$) [36], where the abnormal behavior was correlated to local structural distortion. In the case of TiS_3 , our theoretical calculations show that the separation of the dangling S_2 pair ($d_{\text{S-S}}$) changes gradually from $<a/2$ to $>a/2$ upon compression. The increase in $d_{\text{S-S}}$ means a softening of the S_2 pair vibration, leading to the unusual negative pressure dependence of the related Raman-active mode [16]. Meanwhile, the softening of the S_2 pair vibration indicates that the lattice a is somewhat resistive to the applied pressure, as manifested by the unexpected increase of a/b with increasing P [bottom frame of Fig. 4], despite that the bonding along the a axis is much weaker than that along the b axis. The abnormal increase in $d_{\text{S-S}}$ under high pressure should also influence the transport properties by reducing the overlap of the electronic orbitals between S_2 pair, which

might be the reason of the unusual insulating state.

IV. CONCLUSIONS

In summary, we have investigated the high-pressure electric and structural properties of TiS_3 single crystal. As the pressure is increased from ambient to $P_{C1} \sim 12$ GPa, the original semiconducting behavior becomes more and more insulating. At the critical pressure of P_{C1} , extremes in the lattice parameters ratios are observed consistently. We argue that the softening of dangling S_2 pair along a axis might contribute to these abnormal behaviors. Upon further compression, both the XRD and theoretical calculations document an iso-symmetric structural transition at P_{C2} , mainly referred to rearrangement of the S_2 pair along the a axis. Accompanied by the structural transition, a pressure-induced semiconductor-to-metal transition is observed.

ACKNOWLEDGEMENTS

We thank for the financial support from the National Key Research and Development Program of China (Grants No. 2016YFA0401804, No. 2016YFA0300404 and No. 2015CB921202), the NSFC (Grants No. U1632275, No. 11574323, No. 51372112, No. 11574133), the NSF of Anhui Province (Grant No. 1708085QA19), the NSF of Jiangsu Province (Grant No. BK20150012), the Director's Fund of Hefei Institutes of Physical Science, CAS (Grant No. YZJJ201621) and Special Program for Applied Research on Super Computation of the NSFC-Guangdong Joint Fund (the second phase). Some of the calculations were performed on the supercomputer in the HPCC of Nanjing University and "Tianhe-2" at NSCC-Guangzhou. The X-ray work was performed at HPCAT (Sector 16), Advanced Photon Source, Argonne National Laboratory. HPCAT operations are supported by DOE-NNSA under Award No. DE-NA0001974 and DOE-BES under Award No. DE-FG02-99ER45775, with partial instrumentation funding by NSF. The Advanced Photon Source is a U.S. Department of Energy (DOE) Office of Science User Facility operated for the DOE Office of Science by Argonne National Laboratory under Contract No. DE-AC02-06CH11357.

C. An and P.C. Lu contributed to this work equally.

Reference

- [1] A. J. Molina-Mendoza, M. Barawi, R. Biele, E. Flores, J. R. Ares, C. Sánchez, G. Rubio-Bollinger, N. Agraït, R. D'Agosta, I. J. Ferrer, and A. Castellanos-Gomez, *Adv. Electron. Mater.* **1**, 1500126 (2015).
- [2] J. Dai, and X. C. Zeng, *Angew. Chem. Int. Ed.* **54**, 7572 (2015).
- [3] J. O. Island, M. Barawi, R. Biele, A. Almazan, J. M. Clamagirand, J. R. Ares, C. Sanchez, H. S. van der Zant, J. V. Alvarez, R. D'Agosta, I. J. Ferrer, and A. Castellanos-Gomez, *Adv. Mater.* **27**, 2595 (2015).
- [4] A. J. Molina-Mendoza, J. O. Island, W. S. Paz, J. M. Clamagirand, J. R. Ares, E. Flores, F. Leardini, C. Sánchez, N. Agraït, G. Rubio-Bollinger, H. S. J. van der Zant, I. J. Ferrer, J. J. Palacios, and A. Castellanos-Gomez, *Adv. Funct. Mater.* **27**, 1605647 (2017).
- [5] Y. D. Jin, X. X. Li, and J. L. Yang, *Phys. Chem. Chem. Phys.* **17**, 18665 (2015).
- [6] E. Guilmeau, D. Berthebaud, P. R. N. Misse, S. Hébert, O. I. Lebedev, D. Chateigner, C. Martin, and A. Maignan, *Chem. Mater.* **26**, 5585 (2014).
- [7] P. Misse, D. Berthebaud, O. Lebedev, A. Maignan, and E. Guilmeau, *Materials* **8**, 2514 (2015).
- [8] I. J. Ferrer, M. D. Maciá, V. Carcelén, J. R. Ares, and C. Sánchez, *Energy Procedia* **22**, 48 (2012).
- [9] G. L. Holleck, and J. R. Driscoll, *Electrochim. Acta* **22**, 647 (1977).
- [10] J. O. Island, R. Biele, M. Barawi, J. M. Clamagirand, J. R. Ares, C. Sanchez, H. S. van der Zant, I. J. Ferrer, R. D'Agosta, and A. Castellanos-Gomez, *Sci. Rep.* **6**, 22214 (2016).
- [11] J. Kang, and L. W. Wang, *Phys. Chem. Chem. Phys.* **18**, 14805 (2016).
- [12] K. F. Mak, C. Lee, J. Hone, J. Shan, and T. F. Heinz, *Phys. Rev. Lett.* **105**, 136805 (2010).
- [13] B. Robert, F. Eduardo, R. A. Jose, S. Carlos, J. F. Isabel, R. B. Gabino, C. G. Andres, and D. A. Roberto, arXiv:1509.00532v1.

- [14] M. Li, J. Dai, and X. C. Zeng, *Nanoscale* **7**, 15385 (2015).
- [15] J. Kang, H. Sahin, H. D. Ozaydin, R. T. Senger, and F. M. Peeters, *Phys. Rev. B* **92**, 075413 (2015).
- [16] K. D. Wu, E. Torun, H. Sahin, B. Chen, X. Fan, A. Pant, D. Parsons Wright, T. Aoki, F. M. Peeters, E. Soignard, and S. Tongay, *Nat. Commun.* **7**, 12952 (2016).
- [17] H. Haraldsen, A. Khekshus, E. Rost, and A. Steffensen, *Acta Chem. Scand.* **17**, 1283 (1963).
- [18] L. Brattas, and A. Kjekshus, *Acta Chem. Scand.* **26**, 3441 (1972).
- [19] C. Park, D. Popov, D. Ikuta, C. L. Lin, C. Kenney-Benson, E. Rod, A. Bommannavar, and G. Shen, *Rev. Sci. Instrum.* **86**, 072205 (2015).
- [20] C. Prescher, and V. B. Prakapenka, *High Pressure Res.* **35**, 223 (2015).
- [21] B. A. Hunter, Rietica—A Visual Rietveld Program, International Union of Crystallography Commission on Powder Diffraction Newsletter No. 20 (Summer 1998), <http://www.rietica.org>.
- [22] H. K. Mao, J. Xu, and P. M. Bell, *J. Geophys. Res.* **91**, 4673 (1986).
- [23] G. Kresse, and J. Furthmüller, *Phys. Rev. B* **54**, 11169 (1996).
- [24] J. P. Perdew, K. Burke, and M. Ernzerhof, *Phys. Rev. Lett.* **77**, 3865 (1996).
- [25] S. Grimme, *J. Comput. Chem.* **27**, 1787 (2006).
- [26] G. R. Qian, X. Dong, X. F. Zhou, Y. Tian, A. R. Oganov, and H. T. Wang, *Comput. Phys. Commun.* **184**, 2111 (2013).
- [27] A. R. Oganov, and C. W. Glass, *J. Chem. Phys.* **124**, 244704 (2006).
- [28] A. Togo, F. Oba, and I. Tanaka, *Phys. Rev. B* **78**, 134106 (2008).
- [29] I. G. Gorlova, S. G. Zybtev, and V. Y. Pokrovskii, *JETP Lett.* **100**, 256 (2014).
- [30] S. Klotz, J.-C. Chervin, P. Munsch, and G. Le Marchand, *J. Phys. D: Appl.*

Phys. **42**, 075413 (2009).

- [31] F. Birch, Phys. Rev. **71**, 809 (1947).
- [32] A. Polian, M. Gauthier, S. M. Souza, D. M. Trichês, J. Cardoso de Lima, and T. A. Grandi, Phys. Rev. B **83**, 113106 (2011).
- [33] O. Gomis, R. Vilaplana, F. J. Manjón, P. Rodríguez-Hernández, E. Pérez-González, A. Muñoz, V. Kucek, and C. Drasar, Phys. Rev. B **84**, 174305 (2011).
- [34] Y. H. Zhang, Y. Li, Y. M. Ma, Y. W. Li, G. H. Li, X. C. Shao, H. Wang, T. Cui, X. Wang, and P. W. Zhu, Sci. Rep. **5**, 14681 (2015).
- [35] Y. S. Zhao, W. G. Yang, N. N. Li, Y. Li, R. L. Tang, H. Li, H. Y. Zhu, P. W. Zhu, and X. Wang, J. Phys. Chem. C **120**, 9436 (2016).
- [36] O. B. Korneta, S. Chikara, S. Parkin, L. E. DeLong, P. Schlottmann and G. Cao, Phys. Rev. B **81**, 045101 (2010).

Figures and captions

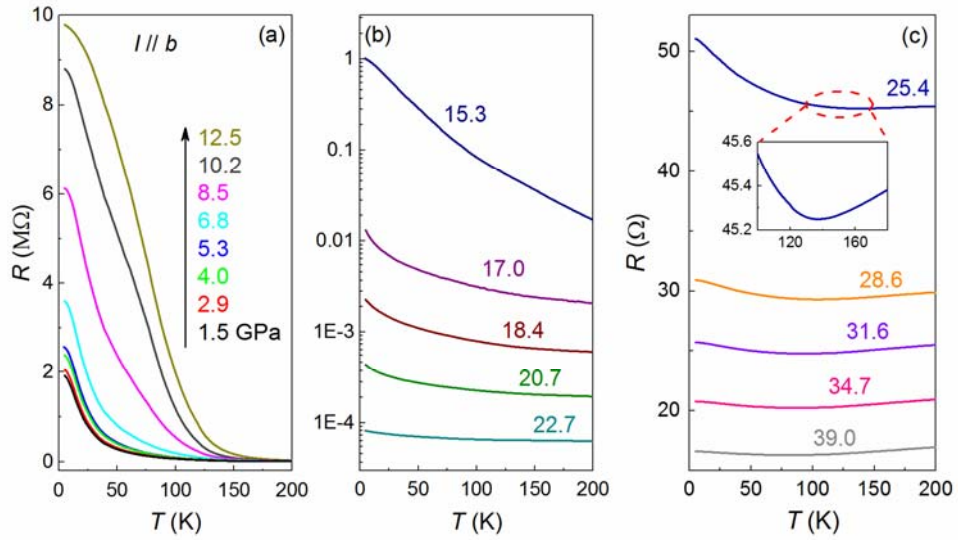


FIG. 1. (Color online) Resistance (R) versus temperature (T) curves in the pressure range of 1.5-12.5 GPa (a), 15.3-22.7 GPa (b) and 25.4-39.0 GPa (c). The current (I) is introduced along the b axis of the single crystal. Note that upon compression the resistance increases increasingly at first until 12.5 GPa, then it decreases rapidly but still with insulating behavior ($dR/dT < 0$). And finally above 25.4 GPa, a metallic behavior [$dR/dT > 0$, inset of Fig. 1(c)] emerges and grows more and more evident up to 39.0 GPa, the highest pressure studied here.

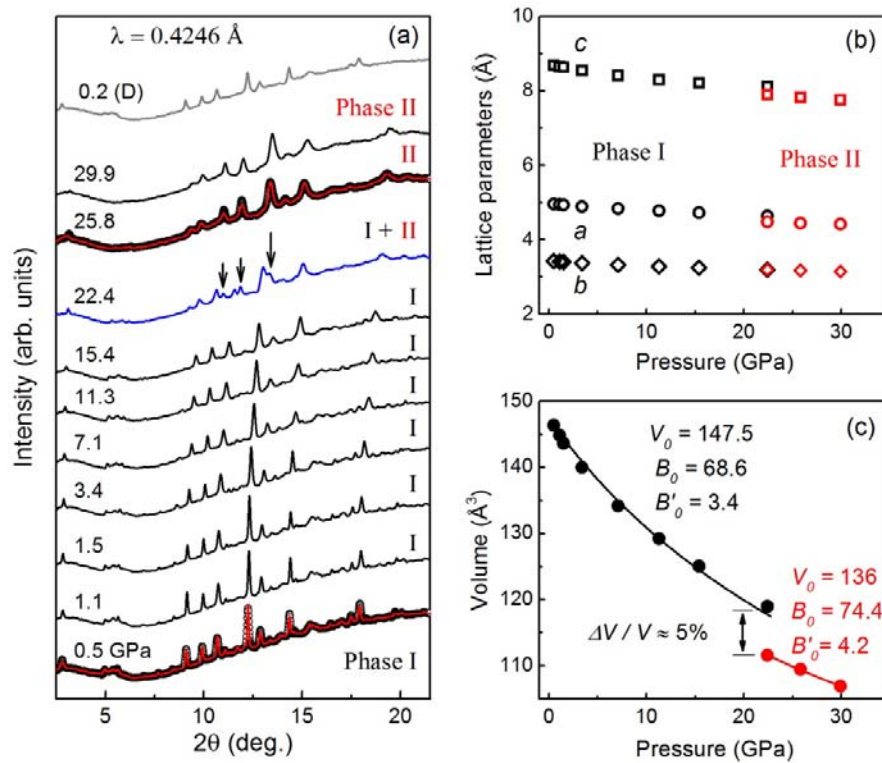


FIG. 2. (Color online) (a) Synchrotron x-ray diffraction patterns of TiS₃ with pressures up to 29.9 GPa ($\lambda = 0.4246 \text{ \AA}$). Some new peaks at 22.4 GPa indicated by arrows evidence a structural transition. Standard Rietveld refinements with Le Bail method were used to fit the experimental data. Selected fitting results (red lines) at 0.5 GPa (Phase I) and 25.8 GPa (Phase II) are included. The XRD pattern upon decompression back to 0.2 GPa (denoted by D) is almost the same as the initial one at 0.5 GPa, manifesting a reversible structural transition. (b) Pressure dependence of the lattice parameters. (c) The unit cell volume versus pressure was fitted by the third-order Birch-Murnaghan formula (solid lines, see text).

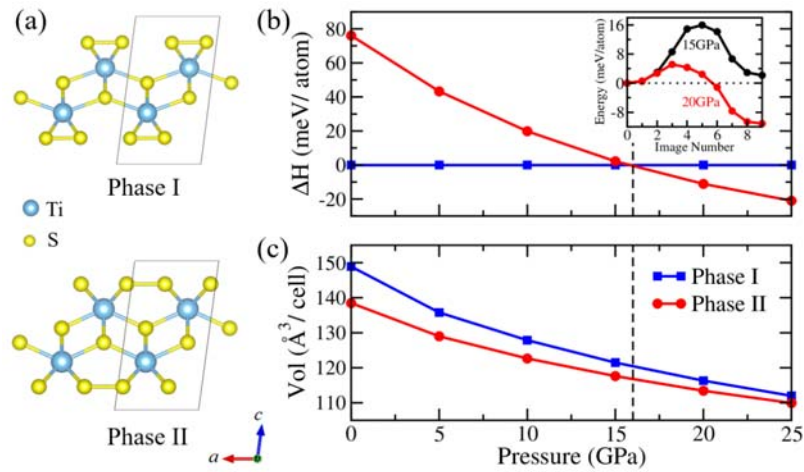


FIG. 3. (Color online) (a) Schematic representations of the ambient structure (Phase I) and the high-pressure structure (Phase II) of TiS₃ along *b* axis. (b) Calculated enthalpy difference between these two phases as a function of pressure. The inset shows the transition barrier from Phase I to Phase II at 15 GPa (black) and 20 GPa (red). (c) Unit cell volume of these two optimized structures vs. pressure. Theoretical calculations indicate an iso-symmetric structural phase transition occurring in TiS₃ at about 16 GPa, from ambient-pressure Phase I to high-pressure Phase II.

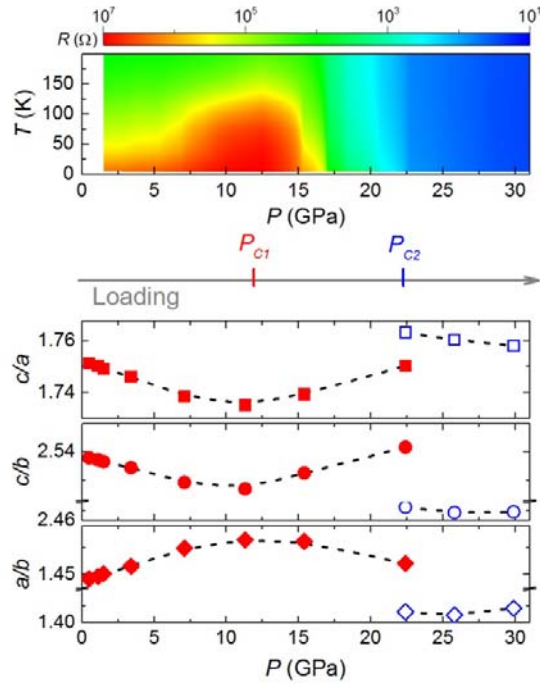


FIG. 4. (Color online) Resistance of single crystal TiS_3 under P - T conditions and its relations to the axial ratios of c/a , c/b and a/b . It is readily drawn that there are two critical pressure points as increasing the pressure: the first one is $P_{C1} \sim 12$ GPa, where the insulating behavior of semiconductor TiS_3 reaches a maximum and all of the axial ratios show extreme points consistently; the second one is $P_{C2} \sim 22$ GPa, where metallization emerges accompanied by discontinuities of the axial ratios due to a structural transformation.

TABLE I. The calculated atomic positions of TiS_3 at 0 and 30 GPa.

Space group	Pressure (GPa)	Atoms	Site	Wyckoff positions		
				x	y	z
$P2_1/m$ (Phase I)	0	Ti1	2e	0.28420	0.25000	0.15171
		S1	2e	0.12148	0.75000	0.32528
		S2	2e	0.23809	0.75000	0.94957
		S3	2e	0.47024	0.25000	0.67824
$P2_1/m$ (Phase II)	30	Ti1	2e	0.29336	0.25000	0.17989
		S1	2e	0.06252	0.75000	0.35259
		S2	2e	0.23768	0.75000	0.94761
		S3	2e	0.39601	0.25000	0.64889

APPENDIX A: STRUCTURAL CHARACTERIZATION

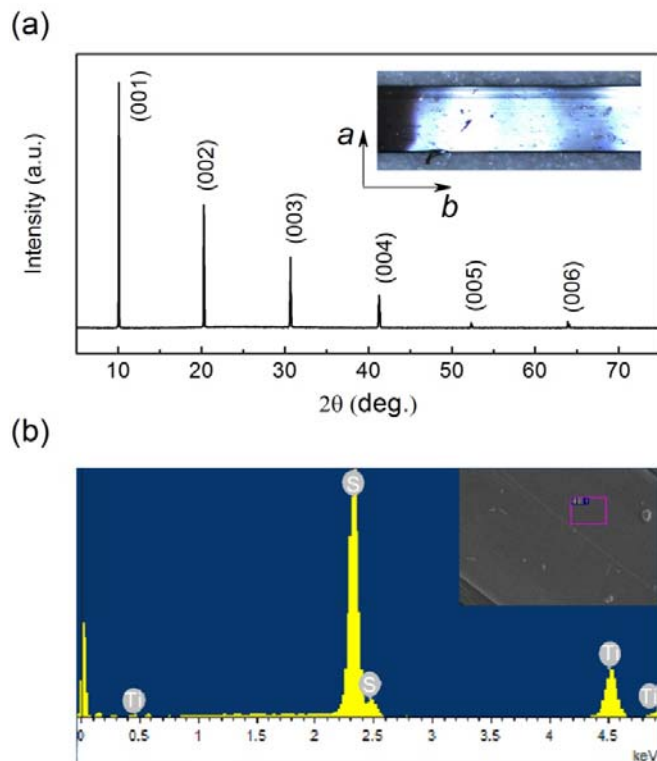


FIG. S1. (Color online) (a) X-ray diffraction pattern of TiS_3 single crystal. The upper right panel shows the photo of TiS_3 single crystal. (b) Energy dispersive x-ray spectroscopy of TiS_3 single crystal.

Stoichiometric Ti and S powders were ground together and loaded into a quartz tube with a small amount of I_2 (transport agent). The tube was sealed under vacuum and placed in a two-zone furnace. The hot zone was maintained at 560 $^\circ\text{C}$ for 10 days and the cold zone was maintained at 470 $^\circ\text{C}$. Belt-like crystals [inset of Fig. S1(a)] with a typical dimension of 10 mm \times 2 mm \times 0.2 mm was obtained on the cold end. EDX spectra [Fig. S1(b)] with area and point scanning modes give that the value of Ti:S is $\sim 1:3.05$.

APPENDIX B: PHONON DISPERSION CALCULATION

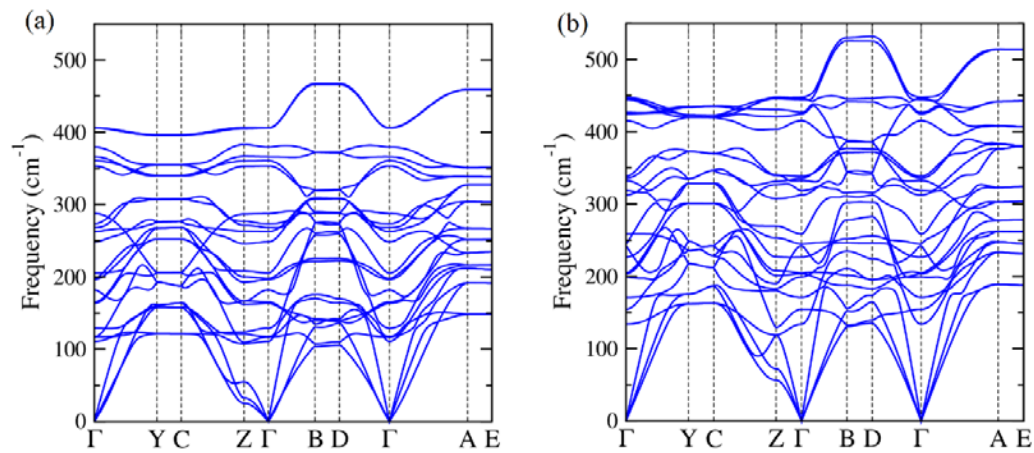


FIG. S2. Calculated phonon dispersion relations of Phase II at (a) 0 GPa and (b) 20 GPa.